



The ∞ Galaxy: A Candidate Direct-collapse Supermassive Black Hole between Two Massive, Ringed Nuclei

Pieter van Dokkum^{1,2} , Gabriel Brammer³ , Josephine F. W. Baggen¹, Michael A. Keim¹ , Priyamvada Natarajan¹ , and Imad Pasha^{1,2}

¹ Astronomy Department, Yale University, 219 Prospect Street, New Haven, CT 06511, USA

² Dragonfly Focused Research Organization, 150 Washington Avenue, Suite 201, Santa Fe, NM 87501, USA

³ Cosmic Dawn Center (DAWN), Niels Bohr Institute, University of Copenhagen, Jagtvej 128, København N, DK-2200, Denmark

Received 2025 April 13; revised 2025 May 16; accepted 2025 May 18; published 2025 July 15

Abstract

We report the discovery of an unusual $z = 1.14$ object, dubbed the ∞ galaxy, in JWST imaging of the COSMOS field. Its rest-frame near-IR light is dominated by two compact nuclei with stellar masses of $\sim 10^{11} M_{\odot}$ and a projected separation of 10 kpc. Both nuclei have a prominent ring or shell around them, giving the galaxy the appearance of a figure eight or an ∞ symbol. The morphology resembles that of the nearby system II Hz 4, where the head-on collision of two galaxies with parallel disks led to the formation of collisional rings around both of their bulges. Keck spectroscopy, Very Large Array radio data, and Chandra X-ray data show that the ∞ galaxy hosts an actively accreting supermassive black hole (SMBH) with quasar-like radio and X-ray luminosity. Remarkably, the SMBH is not associated with either of the two nuclei but is in between them in both position and radial velocity. Furthermore, from excess emission in the NIRCAM F150W filter, we infer that the SMBH is embedded in an extended distribution of H α -emitting gas, with a rest-frame equivalent width ranging from 400 Å to 2000 Å. The gas spans the entire width of the system and was likely shocked and compressed at the collision site in a galaxy-scale equivalent of what happened in the bullet cluster. We suggest that the SMBH formed within this gas in the immediate aftermath of the collision, when it was dense and highly turbulent. If corroborated with simulations and follow-up JWST spectroscopy, this would demonstrate that “direct” SMBH formation by a runaway gravitational collapse is possible in extreme conditions.

Unified Astronomy Thesaurus concepts: Supermassive black holes (1663); Active galaxies (17)

1. Introduction

The James Webb Space Telescope (JWST) has enabled us to find and study galaxies that were beyond the reach of previous observatories. This is most obviously the case at the highest redshifts, with JWST having found galaxies out to $z \sim 14$ (E. Curtis-Lake et al. 2023; S. Carniani et al. 2024) and uncovering previously unknown populations of red galaxies at $z \sim 6$ –10 (I. Labbé et al. 2023; J. Matthee et al. 2024). JWST is also providing qualitatively new information at lower redshifts, even for relatively bright objects, because of its exquisite spatial resolution, sensitivity, access to wavelengths beyond $2 \mu\text{m}$, and spectroscopic capabilities (see, e.g., L. Mowla et al. 2022; E. J. Nelson et al. 2023; R. Jain & Y. Wadadekar 2024; A. G. Beverage et al. 2025, for some examples).

In this context, it is worthwhile to search for unusual objects in public wide-field JWST surveys, even in areas of the sky that have been studied extensively in prior Hubble Space Telescope (HST) programs. One of the first such surveys was COSMOS-Web (C. M. Casey et al. 2023), a multiband NIRCAM program in the COSMOS field (N. Scoville et al. 2007). Any objects found in this area of the sky have a wealth of data available at other wavelengths, especially in the part of the field that coincides with the CANDELS survey (A. M. Koekemoer et al. 2011; I. G. Momcheva et al. 2016).

Two of us (G.B. and P.v.D.) conducted a search for interesting objects in the COSMOS-Web NIRCAM data by visually inspecting a mosaic of the reduced data.⁴ Several objects stood out to us. The first was a complete Einstein ring around a compact, massive galaxy at $z \approx 2$, presented in P. van Dokkum et al. (2024). The Einstein ring was independently identified by the COSMOS-Web team (W. Mercier et al. 2024).

The second is shown in Figure 1 and is the subject of this Letter. It has a highly unusual morphology: two very compact, red nuclei, each surrounded by a conspicuous ring or shell.⁵ We nicknamed the object the ∞ galaxy because of its dual-ring morphology at rest-frame optical wavelengths. Follow-up observations, detailed below, showed that the galaxy is at $z = 1.14$ and that it hosts an active supermassive black hole (SMBH) in between the two nuclei.

2. Data

2.1. Description of the HST and JWST Imaging

The ∞ galaxy is at $10^{\text{h}}00^{\text{m}}14^{\text{s}}189, +2^{\circ}13'11''.67$ (J2000) in the CANDELS/3D-HST area of the COSMOS field (I. G. Momcheva et al. 2016). We reduced JWST NIRCAM and MIRI imaging from the Cosmos-Web (C. M. Casey et al. 2023) and PRIMER (C. T. Donnan et al. 2024) surveys with the imaging module of the *grizli* code (G. Brammer 2023),

⁴ <https://github.com/gbrammer/grizli-notebooks/tree/main/JWST>

⁵ We initially thought that the ∞ galaxy was a single galaxy with a ring on the edges of two adjacent exposures and that an astrometry problem had rendered it twice in the mosaic.

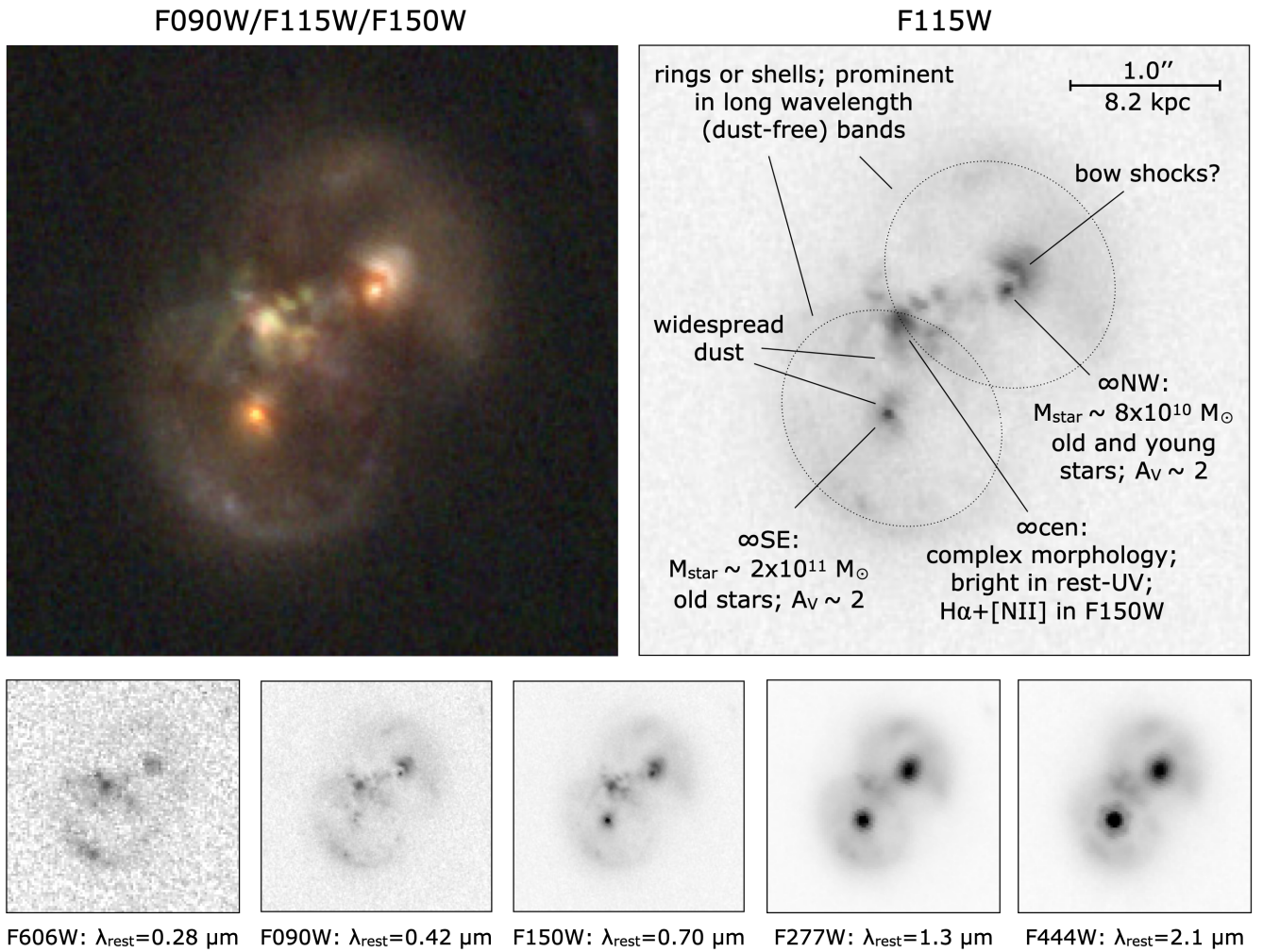


Figure 1. JWST and HST images of the ∞ galaxy. The top left panel shows a color image created from JWST/NIRCAM F090W, F115W, and F150W data, sampled at $0''.02 \text{ pixel}^{-1}$. Key morphological elements are indicated in the F115W rendition at top right. The row of small panels at the bottom shows the appearance of the object in selected HST/ACS and JWST/NIRCAM bands. In the rest-frame K band, the flux is dominated by two bright and compact nuclei, each with an apparent ring or shell around it.

sampled at a resolution of $0''.02 \text{ pixel}^{-1}$ (NIRCAM, short wavelength channel) or $0''.04 \text{ pixel}^{-1}$ (NIRCAM, long wavelength channel, and MIRI). The small panels of Figure 1 show single-band images of the galaxy at different wavelengths. Red, green, and blue (RGB) color images ranging from HST Advanced Camera for Surveys (ACS) F606W all the way to JWST/MIRI F1800W are shown in Figure 2.

The F277W, F356W, and F444W filters sample the rest-frame near-IR and are not very sensitive to dust, emission lines, or young stars. The nuclei and the rings are prominent in these filters, with little color variation between them. This shows that the rings are stellar and that their separation from the nuclei at shorter wavelengths is not caused by radial gradients in dust extinction. In between the rings is a compact region that is bright in the rest-frame UV and in several JWST bands. It is particularly bright in F150W, which contains the redshifted $H\alpha$, $[\text{N II}]$, and $[\text{S II}]$ lines. This excess F150W emission is conspicuous in the F090W/F150W/F277W RGB image as it shows up as green. The northwest (NW) nucleus is relatively bright in the MIRI F1800W filter. This filter samples the rest-frame $8 \mu\text{m}$ polycyclic aromatic hydrocarbon (PAH) emission band.

2.2. Keck Spectroscopy

2.2.1. Observations and Data Reduction

The ∞ galaxy was observed with LRIS on the Keck I telescope on three occasions, 2023 April 24, 2024 November 7, and 2024 November 27. For all observations, we used the $300 \text{ lines mm}^{-1}$ grism, blazed at 5000 \AA , in the blue and the 6800 \AA dichroic. Other settings are listed in Table 1. The 2023 data are relatively shallow, but they cover a large wavelength range and include the important redshifted $H\beta$ and $[\text{O III}]$ lines.

The data were reduced using a combination of standard packages and custom techniques. We used `PyEIT` (J. Prochaska et al. 2020) to generate a sky model, identify cosmic rays, and fit an approximate wavelength solution for each frame. The code was run in the AB subtraction mode for the red side data of 2024 November 28 to optimize sky subtraction. All other data were reduced in the normal reduction mode. This served as the basis for tailored reduction steps. We used sky emission lines to correct the wavelength solutions in all individual frames. This was particularly important for the data beyond $1 \mu\text{m}$ in 2023, where the standard reduction produced significant errors. The spectra were then placed on a common wavelength grid. Next, the 2D spectra were corrected for s -distortion by determining the location

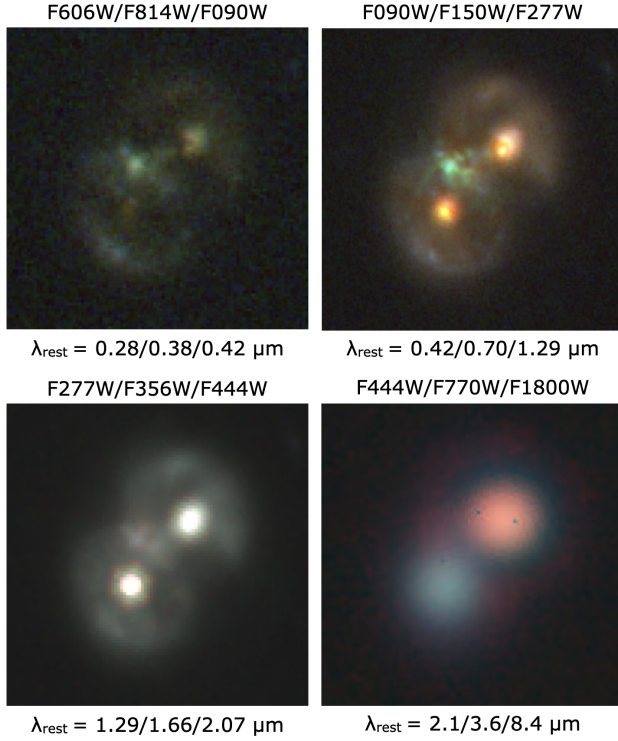


Figure 2. Top left: HST/ACS F606W and F814W and JWST/NIRCAM F090W, with the F090W image smoothed to the HST resolution. Top right: JWST/NIRCAM F090W, F150W, and F277W. Bottom left: JWST/NIRCAM F277W, F356W, and F444W. Bottom right: JWST/NIRCAM F444W, JWST/MIRI F770W, and JWST/MIRI F1800W, with F444W and F770W smoothed to the F1800W resolution.

Table 1
LRIS Observations

Date	Grism	Grating	t_{exp} (s)	PA (deg)
2023 Apr 24	300/5000	400/8500	1800	−60
2024 Nov 11	300/5000	600/10,000	4500	−17
2024 Nov 27	300/5000	600/10,000	8400	−45

of the spectral trace as a function of wavelength and shifting the spectra in the spatial direction. Finally, a master frame was created as a weighted combination of individual frames. We determined the weights by summing across the wavelength direction and fitting the trace of the brightest object with a Gaussian, taking the ratio of the integrated flux to the FWHM as that frame’s weight. Cosmic-ray masks, reduced together with science frames using the same steps as previously described so that all affected pixels were masked, were utilized in the sum so that the master frame was the weighted average of all nonmasked pixels.

Prior to combining the 2023 and 2024 data, we performed a relative flux calibration. In 2023, no standard star was observed. We obtained a wavelength-dependent flux calibration by fitting the strength of OH emission lines from the night sky to a theoretical spectrum. For the 2024 data, we used observations of the standard star Feige 34 to derive the response function of the instrument. The three data sets were combined by requiring that the average fluxes at $6000 \text{ \AA} < \lambda < 6200 \text{ \AA}$ (blue) and $7000 \text{ \AA} < \lambda < 7200 \text{ \AA}$ (red) are the same for the three data sets.

The shallow 2023 data were only used in the far red, where there is no 2024 coverage. Absolute calibration was performed in the following way. We measured the through-the-slit flux in the HST/ACS F814W image after convolution with an $\text{FWHM} = 1''$ Gaussian. We then integrated the LRIS spectrum over the wavelength range of the F814W filter. The ratio of the F814W flux and the integrated spectral flux gives the calibration factor to bring the spectrum to a calibrated flux density scale.

The combined spectrum is shown in Figure 3. It was extracted from a $1''.1$ region centered on the peak of the emission line flux in the spatial direction. The spectrum is characterized by many strong emission lines, including high-ionization species such as $[\text{Ne V}] \lambda\lambda 3346, 3426$. Remarkably, the reddest detected line ($[\text{O III}] \lambda 5007$) is at an observed wavelength of 10716 \AA , where LRIS has very low sensitivity.

2.2.2. Emission Line Fits

Most of the emission lines are fit with a combination of a Gaussian and a linear function. Inputs are the observed spectrum and an error spectrum. The error spectrum is determined by extracting spectra from empty regions away from the galaxy and determining the rms scatter in these spectra as a function of wavelength. Fits of single lines have four free parameters: the width and normalization of the Gaussian and the slope and offset of the linear function. In most cases, several lines are fit simultaneously, as they are close in wavelength; examples are the $[\text{C III}]$, C III lines and the Mg II doublet. The redshift is held fixed at $z = 1.1403$, as initially determined from a joint fit to all isolated lines. Most of the lines have widths of $\sigma \approx 250 \text{ km s}^{-1}$.

For two lines, we fit more complex functions. The $[\text{Ne III}] \lambda 3869$ line has a clear blue wing that we approximate by fitting a second Gaussian. This second Gaussian has a central wavelength that is blueshifted by $\approx 150 \text{ km s}^{-1}$ and a width $\sigma \approx 350 \text{ km s}^{-1}$. The other line is $\text{H}\gamma$, the only Balmer line that has a reasonably high signal-to-noise ratio. The line appears to have a broad component, although the interpretation is hampered by the fact that the red side of the line suffers from contamination by sky lines. Fitting two Gaussians with fixed centers gives widths of $\sigma = 104 \pm 26 \text{ km s}^{-1}$ for the narrow component and $\sigma = 397 \pm 45 \text{ km s}^{-1}$ for the broad component. The broad component’s flux is $\sim 5\times$ higher than that of the narrow component. We note here that $\text{H}\alpha$ is likely extremely bright (see Figure 2) but not accessible to ground-based spectroscopy as it falls in the H_2O absorption gap between the J and H bands.

2.3. Additional Data

2.3.1. X-Ray Luminosity and Hardness Ratio

The X-ray luminosity is determined from Chandra observations, obtained from the IPAC COSMOS archive (F. Civano et al. 2016). The galaxy is a strong detection with 74 ± 10 counts in the $0.5\text{--}7 \text{ keV}$ band for an exposure time of 16.2 ks. The corresponding flux is $F_{0.5\text{--}7 \text{ keV}} = (4.1 \pm 0.6) \times 10^{-14} \text{ erg s}^{-1} \text{ cm}^{-2}$, where we used the Cycle 8 sensitivity of the ACIS detector. Assuming a power-law spectrum with $\Gamma = 1.8$ (see below), the luminosity in the rest-frame $2\text{--}10 \text{ keV}$ band is $L_X \approx 1.5 \times 10^{44} \text{ erg s}^{-1}$.

With 54 ± 8 counts in the $0.5\text{--}2 \text{ keV}$ band and 19 ± 5 counts in the $2\text{--}7 \text{ keV}$ band, the hardness ratio, $\text{HR} = (\text{H} - \text{S})/(\text{H} + \text{S}) = -0.48 \pm 0.12$, indicates a relatively soft spectrum.

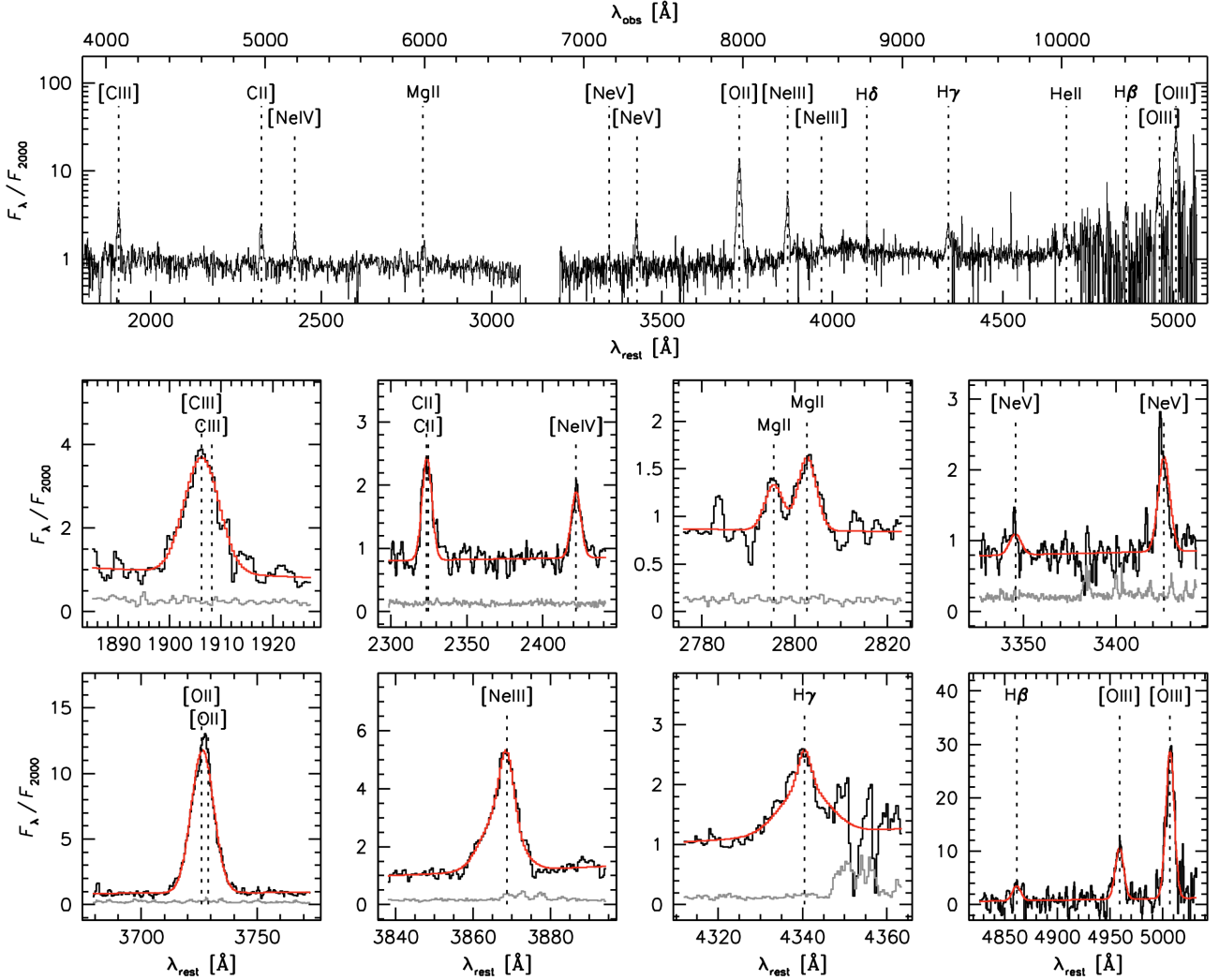


Figure 3. Combined Keck/LRIS spectrum of the ∞ galaxy. The top panel shows the entire wavelength range, with a logarithmic y-axis to capture the large dynamic range of the emission lines. Zoomed views are on a linear scale. Black lines are observations, gray lines indicate the errors, and red lines are Gaussian emission line fits redshifted to $z = 1.1403$. For [Ne III] and $H\gamma$, a second component was fit to model the outflow and broad component, respectively. The spectrum shows a high degree of ionization and resembles that of a narrow-line AGN.

The spectral slope, calculated from the fluxes in the soft and hard bands, is $\Gamma \approx 1.8$.

2.3.2. Radio Observations

The ∞ galaxy is a very strong radio source. Very Large Array (VLA) observations were obtained from the IPAC COSMOS archive. The galaxy has flux densities of $S_\nu = 1.5$ mJy at 1.4 GHz and $S_\nu = 0.43$ mJy at 3 GHz. We also obtain data from the Low-Frequency Array (M. P. van Haarlem et al. 2013) at 144 MHz and measure a flux density of $S_\nu = 23.4$ mJy. We obtain a rest-frame radio luminosity of $L_{144 \text{ MHz}} = 2 \times 10^{26} \text{ W Hz}^{-1}$, where we use a spectral index of $\alpha = 1.3$ ($S_\nu \propto \nu^{-\alpha}$). The spectral index is determined from a fit to the 144 MHz, 1.4 GHz, and 3 GHz flux densities.

Below, we use the centroid of the VLA 3 GHz observation to pinpoint the location of the SMBH within the JWST NIRCAM images. We verify the relative astrometry between the JWST and VLA data in the following way. First, we obtained VLA 3 GHz and HST/ACS F814W data from the IPAC archive in a $4' \times 4'$ field centered on the ∞ galaxy. Sources are detected in both images using SExtractor

(E. Bertin & S. Arnouts 1996), and the centroids of these sources are compared after cross-matching the catalogs. We find nine sources that are bright and compact in the F814W image and the VLA data (besides the ∞ galaxy itself). There is a small systematic offset in position of $-0''.11 \pm 0''.02$ in R.A. and $-0''.01 \pm 0''.02$ in decl. Next, we compare the position of the ∞ galaxy in the IPAC F814W image to that in our reductions. Our reductions show the same offset with respect to the IPAC F814W data as the VLA data do, and we conclude that the VLA 3 GHz map is on the same astrometric system as our HST and JWST reductions, with an accuracy of $\lesssim 0''.04$.

3. Analysis

3.1. Stellar Populations and Sizes of the Two Nuclei

The two red nuclei (marked ∞ southeast (SE) and ∞ NW) dominate the rest-frame near-infrared light. They are remarkable in their own right, as they are very bright and also very compact. We performed stellar population fits to determine approximate stellar masses. Photometry in all available HST and JWST bands was obtained with an automated pipeline

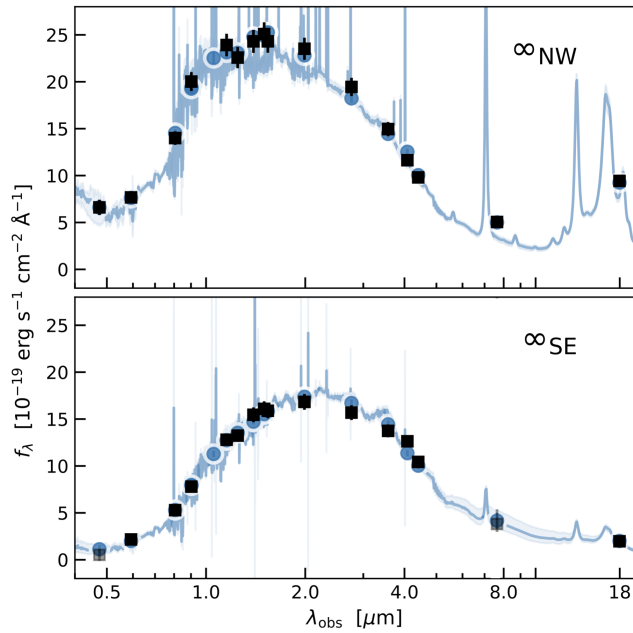


Figure 4. Top: stellar population fit, using the *eazy* code, for ∞ NW. The implied stellar mass is $8 \times 10^{10} M_{\odot}$. Note that the galaxy has strong $8 \mu\text{m}$ PAH emission, sampled in the F1800W MIRI band. Bottom: fit for ∞ SE. This galaxy has a mass of $1.8 \times 10^{11} M_{\odot}$ and is mostly composed of evolved stellar populations. Both galaxies are dusty, with $A_V \sim 2$.

following procedures that have been used for other public JWST imaging surveys (F. Valentino et al. 2023). The two nuclei of the ∞ system were identified as unique sources in the automatic catalog procedure without modification, and their multiwavelength photometry extracted within $D = 0''.5$ circular apertures was fit with the *eazy* code (G. B. Brammer et al. 2008), with the redshift held fixed to $z = 1.14$. The code fits linear combinations of template spectral energy distributions (SEDs) to the observed HST and JWST photometry. The individual templates have a range of star formation histories (with nebular emission from the youngest stellar populations) and dust attenuation; each template has an associated M/L ratio, and the total stellar mass can be estimated from their weights in the fit (I. Labbé et al. 2023). The best-fitting SEDs for the two nuclei are shown in Figure 4.

The NW nucleus is best fit by a mixture of evolved stellar populations, young populations, and ongoing star formation. The F1800W data point requires templates with strong $8 \mu\text{m}$ PAH emission. The mass is $M_{\text{stars}} \sim 8 \times 10^{10} M_{\odot}$, and there is significant dust attenuation with $A_V \sim 2.3$ mag. The SE nucleus is even more massive and older, with low levels of ongoing star formation. We find $M_{\text{stars}} \sim 1.8 \times 10^{11} M_{\odot}$. Its dust attenuation is high for such an old, evolved galaxy, with $A_V \sim 2.1$ mag. There is an obvious dust lane across ∞ SE in the JWST images, and it may be that some or most of the dust is in its local foreground rather than within the nucleus itself.

We fit Sérsic profiles to the F444W images to measure the sizes of the two nuclei using the GALFIT code (C. Y. Peng et al. 2002). Free parameters are the position in the image, the position angle, the effective radius along the major axis (r_e), the Sérsic index (n), and the projected minor-to-major axis ratio (b/a). Circularized effective radii are calculated as $r_{e,c} = r_e \sqrt{b/a}$. To fit the two nuclei, we mask the surrounding complex emission using the following approach. First, the background is estimated using σ -clipped statistics with a filter

size of 5 pixels and the background rms. This background is subtracted from the data and then convolved with a 2D Gaussian kernel with an FWHM of 3 pixels. Next, sources are detected in the convolved, background-subtracted image using a 1σ detection threshold, where σ corresponds to the background rms prior to convolution. The resulting detection is used to create a mask map, where nonzero pixels are ignored by GALFIT during the fitting process.

The NW nucleus is well resolved, with $r_{e,\text{circ}} = 0''.11$, $n = 1.2$, and $b/a = 0.8$. With $z = 1.1403$, the physical half-light radius $r_{e,\text{circ}} = 0.9$ kpc. The best-fit integrated F444W magnitude is $m_{444} = 20.7$. We find that the ∞ SE nucleus is only just resolved, with $r_e = 0''.052$, $b/a = 0.9$, and $m_{444} = 20.5$. The circularized effective radius $r_{e,\text{circ}} = 0.4$ kpc. The effective radius has a systematic uncertainty of 0.1–0.2 kpc, based on a comparison of results using WebbPSF and two empirical point-spread functions (following J. F. W. Baggen et al. 2024).

The high stellar masses and small sizes imply that the nuclei are extraordinarily compact. The ∞ SE nucleus, in particular, is a factor of ~ 6 smaller than expected from the $z = 1$ size–mass relation of quiescent galaxies (A. van der Wel et al. 2014).

3.2. An Active SMBH

The optical spectrum is characterized by strong emission lines that imply a high degree of ionization. With $[\text{O III}]/\text{H}\beta = 10.3 \pm 1.3$ and $[\text{Ne V}]/[\text{Ne III}] = 0.32 \pm 0.04$, the object falls firmly in the active galactic nucleus (AGN) region of diagnostic diagrams that separate star formation from nuclear activity (see N. J. Cleri et al. 2023; J. Negus et al. 2023). Furthermore, the pronounced blue wing of the $[\text{Ne III}]$ line (see Section 2.2.2) is commonly interpreted as an AGN-driven outflow in the narrow-line region (J. R. Mullaney et al. 2013).

The interpretation of the line emission as photoionization by an active SMBH is strongly supported by the radio and X-ray luminosity of the ∞ galaxy. The rest-frame radio luminosity of $L_{144 \text{ MHz}} \sim 2 \times 10^{26} \text{ W Hz}^{-1}$ is comparable to the most powerful radio-loud AGNs in the local Universe (L. K. Morabito et al. 2025). The spectral index is steep, $S_{\nu} \propto \nu^{-1.3}$, an indicator of the early stages of jet evolution in a young (10^4 – 5 yr) AGN (C. P. O’Dea 1998). The X-ray luminosity of $L_X \sim 1.5 \times 10^{44} \text{ erg s}^{-1}$ in the rest-frame 2–10 keV band puts it in the border region between luminous Seyfert galaxies and quasars, and the spectral slope of $\Gamma \approx 1.8$ is typical for unobscured or moderately obscured AGNs (A. Corral et al. 2011).

We can obtain a rough estimate of the black hole mass from the width of the $\text{H}\gamma$ line. As discussed in Section 2.2.2, the line can be fitted with a combination of a narrow component and a dominant broad component, with $\text{FWHM} = 940 \pm 110 \text{ km s}^{-1}$. Combined with the estimated $\text{H}\alpha$ luminosity of $L_{\text{H}\alpha} \sim 3 L_{\text{H}\beta} \sim 3 \times 10^{41} \text{ erg s}^{-1}$, this gives an estimated black hole mass of $M_{\text{BH}} \sim 10^6 M_{\odot}$ (Equation (6) in J. E. Greene & L. C. Ho 2005). We note that we cannot constrain the red wing of the $\text{H}\gamma$ line as it falls on a sky line, and it could be that the blue wing should be modeled as an outflow rather than the short-wavelength half of a symmetric broad component. Furthermore, the black hole mass may be significantly lower if chaotic motions in the surrounding gas contribute to the $\text{H}\alpha$ broadening.

Interestingly, the X-ray luminosity is similar to the Eddington luminosity for a $10^6 M_{\odot}$ black hole ($L_{\text{Edd}} \approx 1.3 \times 10^{44} \text{ erg s}^{-1}$). However, this is indicative only, given the large

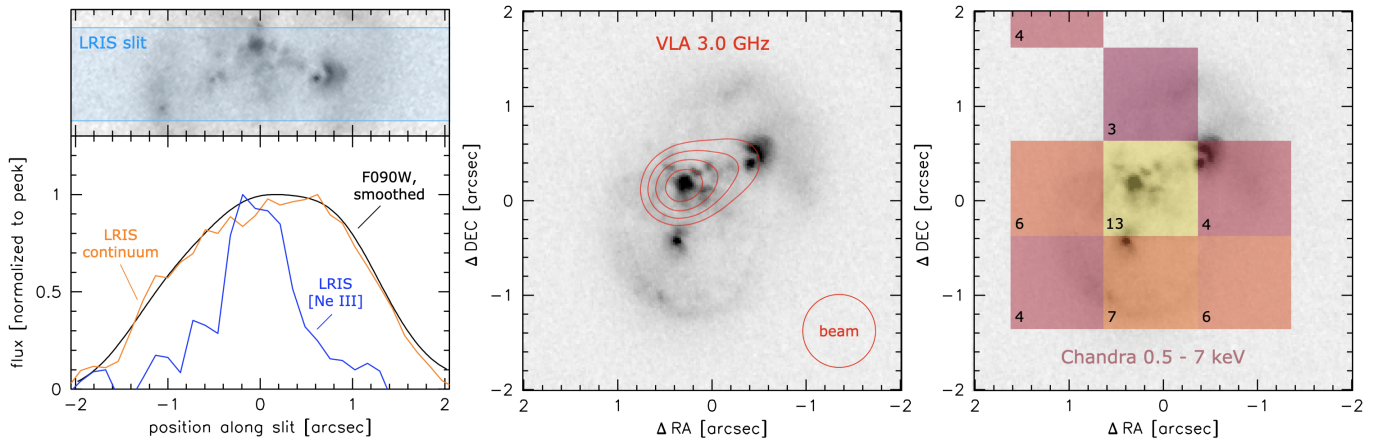


Figure 5. Localization of the active black hole. Left panel: comparison of the spatial profile of the [Ne III] line and the continuum emission along the LRIS slit. The [Ne III] line is unresolved at the LRIS resolution and coincides with the compact ∞ cen region in Figure 1. Middle panel: VLA 3 GHz map, with an FWHM beam of $0''.77$. The strong radio source coincides with ∞ cen to $\lesssim 0''.1$. Right panel: the object is also a strong X-ray source, with $L_X \approx 1.5 \times 10^{44} \text{ erg s}^{-1}$. The number of detected photons is shown in the lower left corner of each Chandra pixel. The pixel containing the ∞ cen region has the highest number of photons. For clarity, pixels with ≤ 2 counts are not shown.

uncertainty in the black hole mass. Furthermore, given the steep spectral index, the X-ray and radio luminosities could be significantly boosted by nonthermal emission from a young jet (see C. P. O’Dea 1998).

3.3. Location of the Black Hole

We now arrive at the most striking and unexpected aspect of the ∞ galaxy: the active SMBH does not appear to be associated with either of the two massive stellar nuclei, as might have been expected, but is located in the complex region in between them (labeled ∞ cen in Figure 1). This is demonstrated in Figure 5, which shows that the high-ionization UV/optical emission lines, the radio emission, and the X-rays all come from this region. The strongest constraint comes from the high spatial resolution VLA 3 GHz map, whose centroid coincides with the brightest pixels of the ∞ cen region to within $\lesssim 0''.1$. We note that there is an extension in the 3 GHz map toward the ∞ NW nucleus; this could be emission from a weak obscured AGN or obscured star formation in that nucleus (D. V. Smirnov et al. 2024) or emission from a jet.

We also identify the likely ionizing source within the ∞ cen region, in the form of a compact blue object that is most clearly seen in the HST F606W band (see Figure 1) at the precise location of the centroid of the 3 GHz map. It may reflect emission from the immediate vicinity of the black hole, such as thermal radiation from the accretion disk or light reprocessed in the broad-line region (J. H. Krolik 1999).

As detailed in Appendix A, we use Galaxy Evolution Explorer (GALEX) imaging to estimate the flux in the rest-frame far-UV and the ionizing photon budget. The ∞ galaxy is clearly detected in the near-UV (NUV) channel at $\lambda_{\text{rest}} \sim 1080 \text{ \AA}$ with a total AB magnitude of 24.7. The galaxy is not resolved at the GALEX resolution of $\approx 5''$, but based on the F606W morphology, as well as ground-based *B*- and *u*-band imaging, it is likely that a considerable fraction of the rest-frame far-UV flux comes from the compact object. We find that the ionizing photon rate is sufficient to produce the observed [O III] luminosity of $L_{[\text{O III}]} \approx 1.2 \times 10^{42} \text{ erg s}^{-1}$ for reasonable photon conversion efficiencies of 0.01–0.1. These values are consistent with the typical ranges seen in AGN

photoionization models and observations (H. Netzer 1990; A. Baskin & A. Laor 2005).

3.4. Radial Velocity of the Black Hole

The SMBH is not only spatially near the center of the ∞ galaxy but also kinematically. It is difficult to measure the radial velocities of the individual components of the galaxy from our ground-based slit spectra given their spatial resolution of $\text{FWHM} \approx 1''.0$. Nevertheless, while the spatial profiles of high-ionization lines such as [Ne III] are consistent with a point source, the [O II] doublet is just resolved in our Keck spectra. The velocity profile along the slit is shown in Figure 6. As seen in the inset, the [O II] emission that is $1''$ – $2''$ away from the black hole coincides with the ring structures and probably reflects ongoing star formation in those regions. There is a gradient from approximately -100 km s^{-1} in the SE to $+100 \text{ km s}^{-1}$ in the NW. The zero-point of the velocity scale is the redshift of the high-ionization lines from the SMBH, and we infer that its radial velocity lies in between that of the two rings.

3.5. Evidence for an Extended Ionized Gas Distribution between the Nuclei

The ∞ cen region has a conspicuous green color in the F090W/F150W/F277W rendition of Figure 2. This can be attributed to the fact that the rest-frame $\text{H}\alpha$, [N II], and [S II] emission lines fall in the F150W filter. We created a continuum image by interpolating between the F090W and F200W filters, $\text{F150W}_{\text{cont}} = 0.44 \times \text{F090W} + 0.56 \times \text{F200W}$. Subtracting the continuum from the F150W image shows the complex line emission in the ∞ cen region (Figure 7). There is a clear peak with a radial falloff, as expected for photoionization by a point rightmost panel of Figure 7 shows the ratio between the line emission map and the continuum, that is, $f \equiv (\text{F150W} - \text{F150W}_{\text{cont}}) / \text{F150W}_{\text{cont}}$. This ratio corresponds to an equivalent width (EW), such that $\text{EW}_{\text{rest}} \approx f \times 1350 \text{ \AA}$. Here EW_{rest} is the rest-frame EW of the sum of $\text{H}\alpha$, [N II], and [S II]. In Figure 8, we show the same map, smoothed by a Gaussian with $\sigma = 0''.02$ and overplotted on the F277W image of the galaxy.

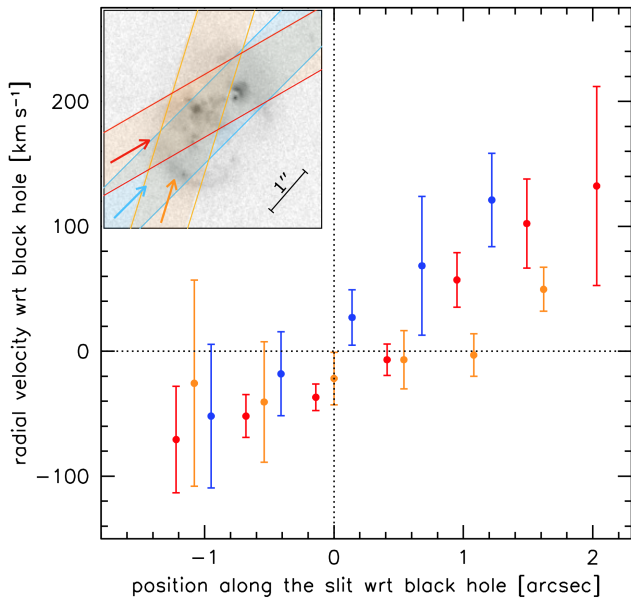


Figure 6. The ∞ galaxy was observed three times with Keck/LRIS, with three different slit angles (see inset). The radial velocity of the low-ionization [O II] doublet is shown as a function of position along the slit, with the positive x -direction indicated by the arrows in the inset. There is a gradient of $\pm 100 \text{ km s}^{-1}$ that is symmetric with respect to the velocity of the highly ionized lines from the SMBH’s narrow-line region. Note that the velocity profile is heavily smoothed by the $1''$ seeing of the observations. The intrinsic profile could be a step function, with each side moving at a constant velocity.

The map shows the luminous and complex $\sim 2 \text{ kpc}$ -sized region around the black hole, with $\text{EW}_{\text{rest}} \sim 1500 \text{ \AA}$. Furthermore, there is line emission with $\text{EW}_{\text{rest}} \sim 400 \text{ \AA}$ in an elongated, $\sim 10 \text{ kpc}$ -sized structure between the two nuclei. The ionized gas distribution is perpendicular to the line between the two nuclei, and the SMBH is embedded within it. We note that, at present, we do not have information on the dynamics or line ratios within the extended ionized gas.

4. Discussion

The ∞ galaxy presents us with not one but two highly unusual observational characteristics. First, we have two massive, extremely compact, red nuclei surrounded by rings or shells; second, we have an SMBH with quasar-like radio and X-ray luminosity sitting in between them.

4.1. What Shaped the ∞ Galaxy?

Turning first to the overall morphology, the ∞ system resembles a pair of collisional ring galaxies, where the head-on impact of a compact galaxy with a disk leads to the sweeping up of disk stars into an outwardly expanding ring. These rings are mostly composed of preexisting disk stars that are herded into similar orbits, combined with young stars that are formed from compressed gas (see, e.g., R. Lynds & A. Toomre 1976; P. N. Appleton & C. Struck-Marcell 1987; L. Hernquist & M. L. Weil 1993; R. J. Smith et al. 2012).

We suggest that ∞ NW and ∞ SE were originally compact, massive bulges that served as mutual impactors in a symmetric collision of two galaxies with disks. The disks would have to have had a nearly face-on orientation with respect to each other. Interestingly, the first collisional ring galaxy that was modeled with N -body techniques, II Hz 4, has a similar binary morphology (R. Lynds & A. Toomre 1976). It was successfully

modeled as a mutual interaction of two disk galaxies, lending support to our interpretation (see Appendix B). Arp 147 is another local example of collisional ring formation around both the impactor and the impacted galaxy, although it does not show the striking symmetry of II Hz 4 or the ∞ galaxy (R. A. Gerber et al. 1992).

The presence of the filamentary gas between the nuclei finds a natural explanation in collision scenarios. The gas in the preexisting galaxies experienced intense shocks and compression at the time of impact and could have partially separated from the stars and dark matter. This process is famously observed in the bullet cluster (D. Clowe et al. 2006), and “minibullet” scenarios have been proposed to explain the formation of dark-matter-free dwarf galaxies (J. Silk 2019; J. Lee et al. 2021; P. van Dokkum et al. 2022). The SMBH is almost certainly responsible for ionizing the gas; the main source is likely photoionization from its UV emission, perhaps augmented by shocks from a jet or wind (e.g., C. M. Harrison et al. 2015). In this scenario, there are not many stars associated with the gas, which explains the extreme EW that is seen in Figure 8. An illustration of the proposed scenario is shown in Figure 9.

4.2. Origin of the SMBH

We now focus on the SMBH that is embedded within the ionized gas in between the two nuclei.

4.2.1. A Third Galaxy?

We first consider the possibility that the black hole is in a third galaxy that is unrelated to the two nuclei. Inspection of the JWST images shows no obvious candidate at the location of the SMBH: the morphology of the ∞ cen region is highly complex, with tendrils of emission extending several kiloparsecs outward from the black hole, and there is no evidence for a bulge, a disk, or other galaxy-like features. Furthermore, the extreme EW of the $\text{H}\alpha + [\text{N II}] + [\text{S II}]$ complex implies that any galaxy light must be unusually faint. The rest-frame EW is $\sim 2000 \text{ \AA}$ at the location of the black hole and remains $\gtrsim 1000 \text{ \AA}$ out to a radius of 2–3 kpc. In contrast, typical AGNs (such as those in the MANGA survey; A. Deconto-Machado et al. 2022) have $\text{EW} \lesssim 100 \text{ \AA}$, due to the significant contribution of the host galaxy’s light to the continuum.

The high radio and X-ray luminosities are difficult to reconcile with a faint dwarf galaxy, as it is highly unusual to see quasar-like activity in a low-mass galaxy (see G. Kauffmann et al. 2003; I. Delvecchio et al. 2022). Nevertheless, the relations between AGN luminosity and galaxy mass, and between inferred black hole mass and galaxy mass, have considerable scatter (Y. Harikane et al. 2023; M. Mezcua et al. 2024), and it is of course difficult to exclude the presence of a low-mass host in the ∞ cen region that is outshone by the SMBH.

4.2.2. An SMBH that Separated from Its Host Galaxy?

Another possible origin for the SMBH is that it was in the center of a galaxy but separated from it, either through ejection from one of the two nuclei or the stripping of an infalling galaxy. Ejections can occur in a variety of dynamical situations (e.g., M. Campanelli et al. 2007). In binary black hole mergers with unequal masses and misaligned spins, large recoil velocities are typically produced due to gravitational radiation, leading to the possible ejection of the final merged black hole

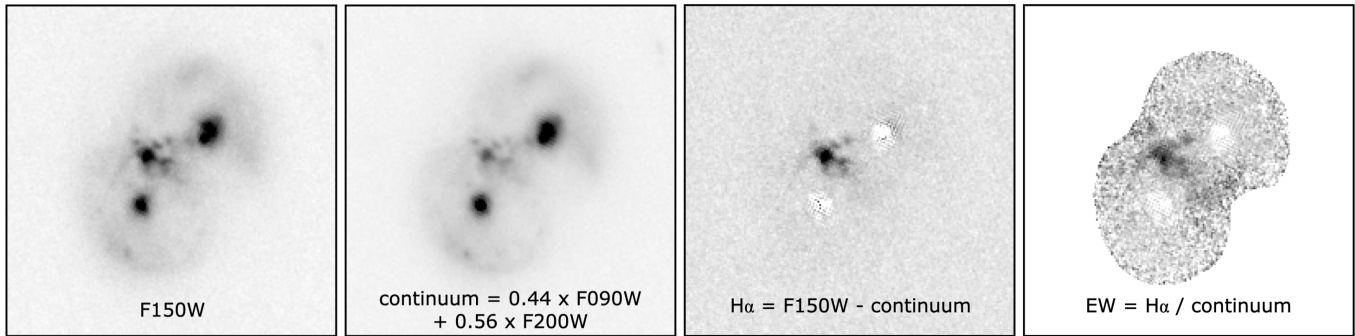


Figure 7. Left: JWST F150W image, containing both continuum and the $H\alpha$, N II, and S II emission lines. Second from left: continuum image, created by interpolating the F090W and F200W images. Second from right: emission line map, created by subtracting the continuum image from the F150W image. Right: EW map, a division of the emission line map by the continuum image.

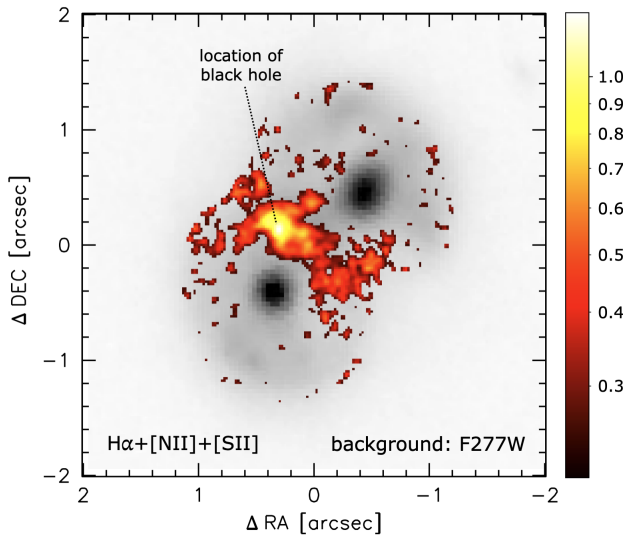


Figure 8. EW map of the $H\alpha + [NII] + [SII]$ line emission in the NIRCAM F150W filter, overplotted on the F277W (rest-frame J) image. The scale bar indicates the strength of the line emission, expressed as a fraction of the F150W continuum. The rest-frame EW is approximately $EW_{\text{rest}} \approx f \times 1350 \text{ \AA}$, with f the continuum fraction. The strong emission line source associated with the black hole is embedded in an elongated ionized gas distribution with a roughly constant EW that is in between the two nuclei.

(C. O. Lousto & Y. Zlochower 2011). Another mechanism for escape is a three-body interaction, when a newly acquired black hole interacts with a preexisting binary black hole. Since galaxies merge frequently and binary black holes are thought to be long-lived, such escapes may be fairly common (J. D. Bekenstein 1973; W. C. Saslaw et al. 1974; L. Hoffman & A. Loeb 2007). Candidates for escaped black holes include the CID-42 double X-ray source in the COSMOS field (F. Civano et al. 2010), a candidate wake of a runaway black hole in the circumgalactic medium of a $z=0.97$ galaxy (P. van Dokkum et al. 2023), and candidates from the Pan-STARRS1 3π Survey (A. Uppal et al. 2024).

Another channel for producing isolated SMBHs is delayed merging. In some cosmological simulations, there is a delay between the infall and final disruption of galaxies and the infall of their SMBHs, producing isolated SMBHs that are typically close to the center of their future host galaxies (M. Tremmel et al. 2018). It has been suggested that these “wandering” black holes can be luminous X-ray sources (A. Ricarte et al. 2021),

and the SMBH may be the remnant on its way to a merger with one of the nuclei.

4.2.3. In Situ Formation?

The scenarios that we discussed so far can, in principle, occur in any galaxy and do not predict a close association between the properties of the SMBH and the (former or future) host galaxy. In both scenarios, the unusual morphology of the ∞ galaxy, the fact that the radial velocity of the SMBH is in between those of the two rings, and its position halfway between the nuclei in an extended ionized gas distribution are all coincidental. Here we discuss a possible origin for the SMBH that is, instead, a *consequence* of the unusual morphology of the system and that also explains its position and radial velocity.

In the minibullet scenario of Section 4.1, the ionized gas in between the nuclei is shocked and compressed due to the recent collision, and it may be that the black hole formed through the runaway gravitational collapse of a cloud or filament within this gas. This scenario links the SMBH to the gas cloud in which it is embedded and explains why its radial velocity is exactly in between the velocities of the gas in the two rings.

This idea is qualitatively similar to “heavy seed” formation models that have long been proposed for the origin of SMBHs in the centers of galaxies. While the leading model for the origin of SMBHs is that they began as the $\sim 10^{1-3} M_{\odot}$ collapsed remnants of the first generation of Population III stars (e.g., P. Madau & M. J. Rees 2001; M. Volonteri et al. 2003), the direct collapse of pregalactic $\sim 10^{4-5} M_{\odot}$ gas clouds is an important alternative (see M. G. Haehnelt & M. J. Rees 1993; D. J. Eisenstein & A. Loeb 1995; V. Bromm & A. Loeb 2003; G. Lodato & P. Natarajan 2006). Simulations show that the lack of metals in these early baryonic objects, combined with external radiation fields and the violent gas dynamics associated with the formation of the halo, can create conditions that are conducive for SMBH formation (G. Lodato & P. Natarajan 2006; P. Natarajan 2011; J. H. Wise et al. 2019). Recently, these models have received renewed attention, as early JWST results are indicating that many galaxies have relatively high black hole masses for their stellar mass (P. Natarajan et al. 2017, 2024; L. J. Furtak et al. 2024; J. E. Greene et al. 2024; J. Matthee et al. 2024).

The similarity to black hole seeding models is only superficial, as the gas in the ∞ galaxy is metal-rich and not at the center of the halo. Recently, the first theoretical studies

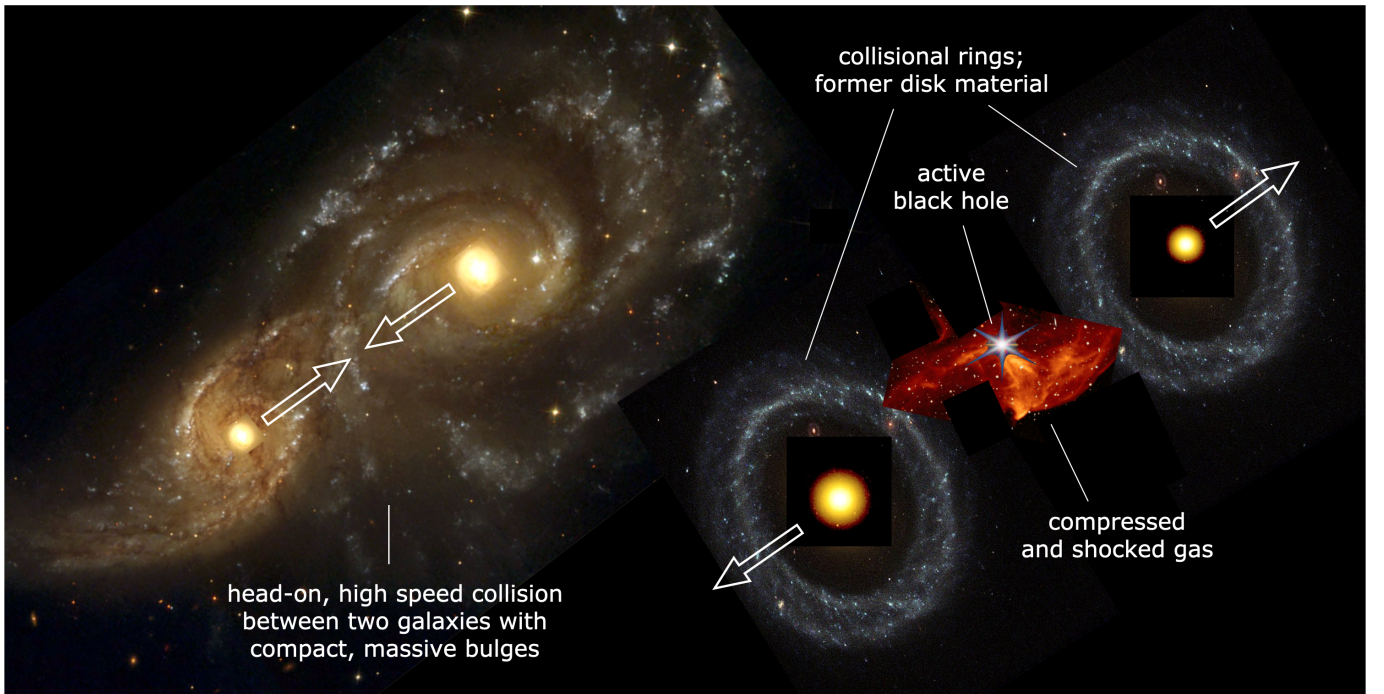


Figure 9. The ∞ galaxy is interpreted as the aftermath of a nearly head-on collision between two face-on disk galaxies with massive, compact bulges. The bulges survived the collision, and the inner disk stars were swept up in outwardly expanding collisional rings around the bulges. The nearby galaxy II Hz 4 is the prototype for this kind of binary ring formation (R. Lynds & A. Toomre 1976). Compression and shocks in the colliding gas likely produced a dense gaseous remnant in between the nuclei, as has been observed in the bullet cluster on much larger scales. It is proposed that the black hole formed within this gas.

of minibullet events have been performed, in the context of forming dark-matter-free dwarf galaxies out of the postcollision gas (J. Silk 2019; E.-j. Shin et al. 2020; J. Lee et al. 2024). While these studies do not have the resolving power to study SMBH formation, they do indicate that regular star formation is suppressed in the turbulent postcollision gas, while the formation of massive self-gravitating clumps is promoted (J. Silk 2019; J. Lee et al. 2021). Furthermore, high-resolution studies of the aftermath of gas-rich mergers have shown that black holes may form in the central regions of the remnant, even though the gas is metal-rich (L. Mayer et al. 2010, 2015). In this formation channel, turbulence and thermal pressure, rather than the absence of metals, prevent fragmentation and star formation. The gas in the ∞ galaxy is currently spread over a ~ 10 kpc region, but it is conceivable that similar extreme conditions were reached locally at the moment of the collision of the two progenitor galaxies.

We note that, in this scenario, both nuclei still have their own, very massive, SMBHs. The stellar velocity dispersions of the nuclei are likely $\sim 300 \text{ km s}^{-1}$ based on their ~ 1 kpc sizes and masses of $\sim 10^{11} M_{\odot}$. The $M_{\text{BH}}-\sigma$ relation implies black hole masses of $\sim 10^9 M_{\odot}$ for dispersions in this range (N. J. McConnell & C.-P. Ma 2013). It would be interesting to look for AGN activity in the two nuclei with sensitive radio or spectroscopic observations, as that could confirm that there are three black holes in the system.

4.3. Geometry of the System and Initial Black Hole Mass

As discussed in Section 4.1, the unusual morphology of the ∞ galaxy can be explained by a face-on collision of two disk galaxies, leading to the formation of collisional rings around the two surviving bulges. In this context, we can use the

observed properties of the galaxy to determine its approximate 3D geometry. Assuming that the rings are intrinsically round, their observed axis ratio of $b/a \approx 0.77$ implies an angle with respect to the plane of the sky of $\approx 40^\circ$. The physical distance between the two nuclei is then ≈ 15 kpc. The proposed geometry along the line of sight is shown in Figure 10.

We can use the deprojected geometry to estimate Δt , the time that has elapsed since collision. The deprojected radial velocity difference between the SE and NW sides of the system is approximately 260 km s^{-1} (see Figure 10), and for a deprojected separation of 15 kpc, this gives $\Delta t \sim 50$ Myr. This time interval is consistent with the typical timescales for collisional ring formation in simulations (C. Struck 2010). The implicit assumption here is that the measured [O II] velocities in the SE and NW are a proxy of the systemic velocities of the ∞ SE and ∞ NW nuclei. This is unlikely to be the case, as the measured line-of-sight velocities of the rings are expected to be a combination of the postcollision velocity of the system, the outward density wave, and the shock dynamics and angular momentum redistribution during the collision (J. L. Higdon 1996). We also assume that the nuclei have not yet turned around and are on their initial postcollision trajectories.

In the context of the direct-collapse model, the elapsed time gives us a rough estimate of the initial mass of the SMBH. For a standard radiative efficiency of $\eta \approx 0.1$, a black hole that accretes at the Eddington rate increases its mass by a factor of ~ 3 over 50 Myr. For a current mass of $10^6 M_{\odot}$, this gives an initial mass of $\sim 3 \times 10^5 M_{\odot}$. We note that, judging from the spectral index, the currently observed episode of black hole activity probably commenced much more recently (see Section 3.2). This indicates that the accretion was probably stochastic over the past ~ 50 Myr.

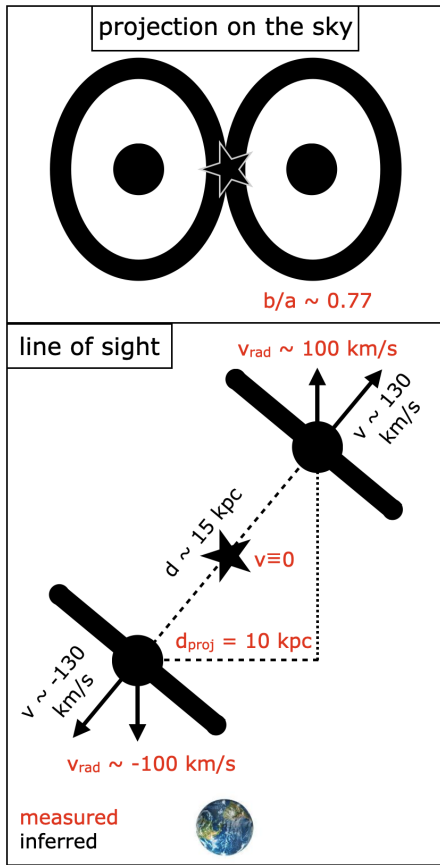


Figure 10. Main panel: possible geometry of the ∞ galaxy along the line of sight. Measured properties are indicated in red and derived properties in black. The orientation is set by the axis ratio of the rings, $b/a \sim 0.77$. Top panel: projection onto the sky. The rings appear to be overlapping but are actually ~ 15 kpc apart.

5. Conclusions

In this Letter, we have presented an unusual galaxy system, consisting of two nuclei with rings in a striking symmetric configuration. In between the nuclei is an SMBH with quasar-like levels of activity that is embedded in a distribution of ionized gas. We suggest that the presence of the SMBH in this system and at that location is not coincidental but the result of a causal chain of events: (1) a nearly face-on collision between two disk galaxies with a small impact parameter, like the one that produced II Hz 4 (see Appendix B); (2) the interaction of gas clouds at the collision site, leading to shocks and compression in a process akin to what is seen in the bullet cluster; (3) the runaway collapse of a dense cloud of gas into a black hole at the collision site; and (4) accretion onto this black hole from the surrounding gas.

The proposal that black holes can form at late times in interacting galaxies is not new; as an example, K. Schawinski et al. (2011) suggested that the presence of several AGNs in a clumpy $z = 1.35$ galaxy could be due to in situ formation and late seeding. The active black hole in the ∞ galaxy stands apart in two important ways: it is perhaps the clearest example yet of an SMBH that is outside of a galaxy nucleus, and we propose a specific mechanism for its formation that can be tested with simulations and follow-up observations.

The minibullet collision can be simulated with strong observational constraints on the postcollision conditions (such

as the positions of the nuclei, the morphology of the rings, the location and morphology of the gas, and the observed radial velocities). It may be that an in-depth analysis of the physical conditions in the colliding clouds will demonstrate that SMBHs cannot form in this scenario. In that case, we are probably witnessing the (re)ignition of a wandering or ejected SMBH as it passes through the gas in the central regions of the ∞ galaxy. If it does turn out to be possible to form black holes, we will learn a lot about the process. For instance, it may be that the collapse is hierarchical, with mergers of massive stars leading to the formation of intermediate-mass black holes and multiple intermediate-mass black holes merging to form the black hole that we now detect (see, e.g., T. Ebisuzaki et al. 2001).

Other tests will come from observations. The spectroscopy presented in this Letter is limited in its spatial resolution and does not cover the key optical emission lines $H\alpha$, $[N II]$, and $[S II]$. These lines are inaccessible from the ground due to H_2O absorption in our atmosphere, but they can be observed with JWST. With the NIRSPEC integral field unit, the presence of the line-emitting gas in between the nuclei could be confirmed, the radial velocities of the nuclei could be measured directly, and the predicted transition between photoionization close to the black hole and shock ionization further out could be observed. Furthermore, any radial velocity offset between the black hole and the surrounding gas could be accurately measured. The most compelling evidence for a runaway gravitational collapse of a clump within this gas would be the observation that there is *no* offset: as noted in Section 4.2.3, this would be difficult to reconcile with a wandering or ejected black hole, and it is a prediction of the in situ formation model.

If our proposed scenario is confirmed, the ∞ galaxy provides an empirical demonstration that direct-collapse formation of SMBHs can happen in the right circumstances—something that has so far only been seen in simulations and through indirect observations (such as high SMBH masses in high-redshift galaxies; L. J. Furtak et al. 2024; J. E. Greene et al. 2024; P. Natarajan et al. 2024; J. Jeon et al. 2025).

Acknowledgments

This Letter uses HST data from program 9822 and JWST data from programs 1837 and 2561, accessible using DOI:10.17909/r5ab-6953. The VLA 3 GHz data are available from V. Smolčić et al. (2020). The notebooks that were used to reduce the data are available as part of the *grizli* package, on Zenodo via DOI:10.5281/zenodo.8370018.

Appendix A Ionizing Flux

The black hole is in the center of the complex ∞ cen region, as determined from the VLA 3 GHz localization. This region is the equivalent of the narrow-line region of an AGN, and we infer from the Keck/LRIS spectrum that it is ionized by highly energetic photons (see Section 3.2). Here we investigate the source of these photons, specifically whether the ∞ cen region has a sufficiently high UV luminosity to produce them. First, we note that there is a compact object at the location of the black hole, within the ∞ cen region. It is blue and most clearly seen in the HST/ACS F606W image of the galaxy (see Figure 1). We suggest that this blue object represents radiation from the accretion disk of the black hole. There are no high-

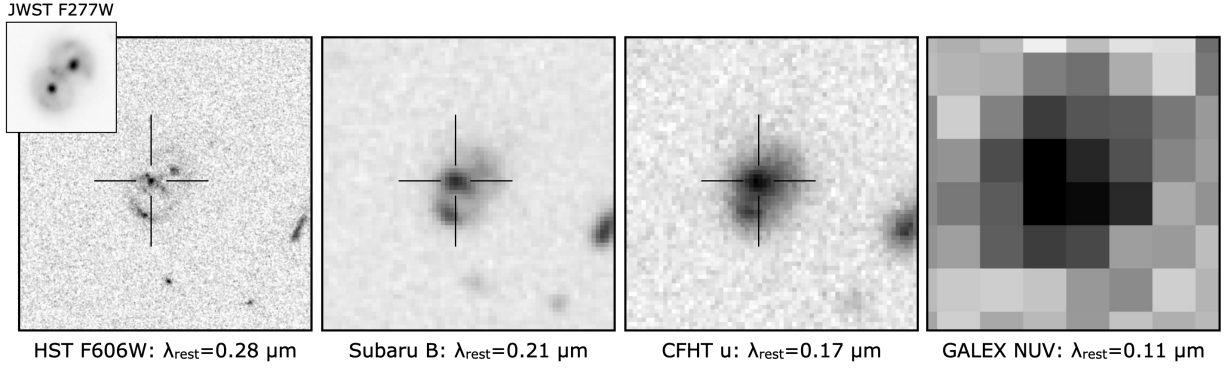


Figure 11. The ∞ galaxy in the rest-frame ultraviolet. From left to right, images at progressively shorter wavelengths are shown. For reference, the inset shows the JWST F277W image ($\lambda_{\text{rest}} = 1.3 \mu\text{m}$). The location of the blue compact object that we associate with the black hole is indicated with a cross. It is bright in the Subaru B and CFHT u bands and likely dominates the GALEX NUV band.

resolution images of the galaxy at shorter wavelengths, but as we show in Figure 11, the ∞ cen region dominates the flux of the entire galaxy in the observed B and u bands at rest-frame wavelengths of $0.21 \mu\text{m}$ and $0.17 \mu\text{m}$, respectively. Remarkably, the galaxy is clearly detected in the GALEX NUV band at $\lambda_{\text{rest}} \approx 0.11 \mu\text{m}$, close to the ionization edge of 912 \AA . The GALEX image is unresolved, but based on the morphology in the B and u bands, it is dominated by the ∞ cen region and plausibly by the compact object within that region.

In the following, we use the observed GALEX NUV flux density to calculate the rate of ionizing photons in the ∞ cen region. Some of the rest-frame far-UV light likely comes from other regions, such as H II regions in the rings or the shock front between the nuclei, which may lead us to overestimate the ionizing flux that is coming from within the ∞ cen region. However, the larger effect is dust, which works in the opposite direction: the intrinsic far-UV luminosity is almost certainly significantly higher than the observed, dust-attenuated luminosity. Given the visible dust lanes in the image (see Figure 1) and the $A_V \sim 2$ attenuation toward the two nuclei, the detected GALEX flux is probably attenuated by a factor of 10–20.

The GALEX NUV AB magnitude $m_{\text{NUV}} = 24.7 \pm 0.1$, corresponding to a rest-frame luminosity density of $L_\nu \approx 1.5 \times 10^{-13} \text{ erg s}^{-1} \text{ Hz}^{-1}$ at $\approx 1100 \text{ \AA}$. The ionization of [O III] requires photons with energy $> 35.1 \text{ eV}$, corresponding to wavelengths $< 352 \text{ \AA}$. The ionizing photon production rate is therefore given by

$$Q = \int_{35.1 \text{ eV}}^{\infty} \frac{L_\nu}{h\nu} d\nu. \quad (\text{A1})$$

Assuming a power law in the UV with $L_\nu \propto \nu^{-1.5}$, this gives $Q \sim 5 \times 10^{53} \text{ photons s}^{-1}$. The [O III] luminosity $L_{[\text{O III}]} = f h \nu_{[\text{O III}]} Q$, with f the fraction of ionizing photons that contribute to [O III]. Comparing this to the observed [O III]

luminosity of $\approx 1.2 \times 10^{42} \text{ erg s}^{-1}$, we find that the GALEX-detected UV source can produce the LRIS-measured line luminosity for $f \sim 0.1$. If the UV source is attenuated by a factor of ~ 10 , then $f \sim 0.01$.

Appendix B

The Binary Collisional Ring Galaxy II Hz 4

The closest known analog to the ∞ galaxy is II Hz 4, a galaxy with two rings and two bulges at $z = 0.043$. We reproduce the deep photographic plate of II Hz 4 obtained by R. Lynds & A. Toomre (1976) in Figure 12, along with the *grz* Legacy survey image of the galaxy (A. Dey et al. 2019). The entire system is larger than the ∞ galaxy, with a total spatial extent along the long axis of $\sim 40 \text{ kpc}$, but is otherwise quite similar. The two bulges and a portion of the bright ring have Sloan Digital Sky Survey spectroscopy (K. Abazajian et al. 2003). The bulges have early-type spectra with $z = 0.04288$ (south) and $z = 0.04295$ (north), respectively. The ring has strong emission lines and $z = 0.04296$. These values are consistent with the original measurements of R. Lynds & A. Toomre (1976), who also note that the northern ring does not have strong emission lines. It would be interesting to obtain further observations of this object.

II Hz 4 was modeled as a mutual collisional system by R. Lynds & A. Toomre (1976) in the first successful N -body simulation done for any ring galaxy.⁶ Lynds & Toomre demonstrated that collisions of bulge + disk systems can lead to the herding of disk stars into outwardly expanding rings around both bulges. In the specific simulation shown in Figure 13, the rotation axes of the disks are parallel to the direction of motion of the galaxies, although the authors note that rings can also be produced if the disks are misaligned by up to 30° . Of greater importance is the impact parameter; to produce a symmetric response, the bulges must pass near each other and interior to most of the disk stars.

⁶ In fact, its binary ring morphology led the authors to the now-standard explanation that collisional rings are caused by a compact impactor.

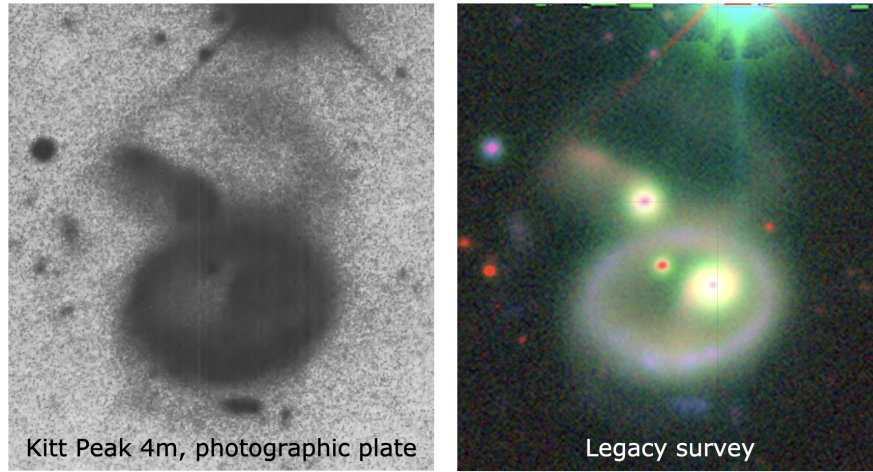


Figure 12. Left: deep photographic plate of the binary ring galaxy II Hz 4, obtained with the Kitt Peak 4 m and reproduced from R. Lynds & A. Toomre (1976). Right: Legacy survey image of the galaxy.

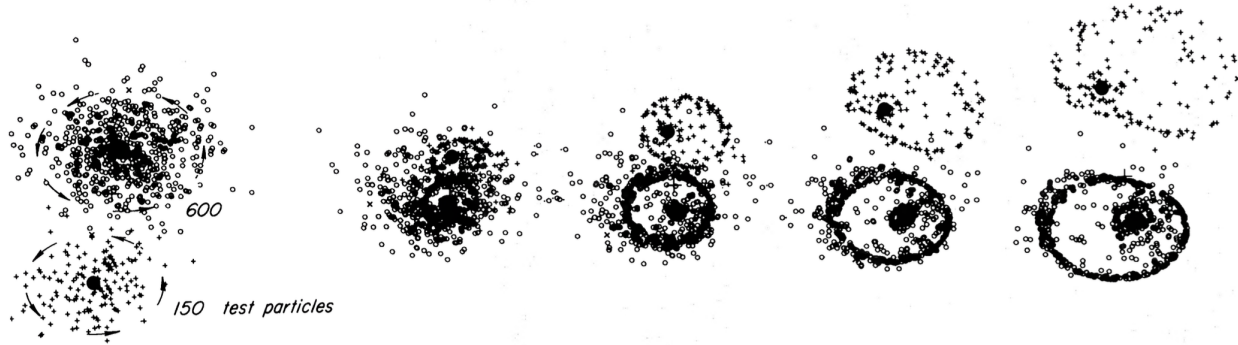


Figure 13. *N*-body simulation of II Hz 4, reproduced from R. Lynds & A. Toomre (1976). In a collision of two bulge + disk galaxies with a small impact parameter, disk stars are herded in outwardly expanding rings around both bulges.

ORCID iDs

Pieter van Dokkum <https://orcid.org/0000-0002-8282-9888>
 Gabriel Brammer <https://orcid.org/0000-0003-2680-005X>
 Michael A. Keim <https://orcid.org/0000-0002-7743-2501>
 Priyamvada Natarajan <https://orcid.org/0000-0002-5554-8896>
 Imad Pasha <https://orcid.org/0000-0002-7075-9931>

References

- Abazajian, K., Adelman-McCarthy, J. K., Agüeros, M. A., et al. 2003, *AJ*, **126**, 2081
 Appleton, P. N., & Struck-Marcell, C. 1987, *ApJ*, **318**, 103
 Baggen, J. F. W., van Dokkum, P., Brammer, G., et al. 2024, *ApJL*, **977**, L13
 Baskin, A., & Laor, A. 2005, *MNRAS*, **358**, 1043
 Bekenstein, J. D. 1973, *ApJ*, **183**, 657
 Bertin, E., & Arnouts, S. 1996, *A&AS*, **117**, 393
 Beverage, A. G., Slob, M., Kriek, M., et al. 2025, *ApJ*, **979**, 249
 Brammer, G. 2023, grizli, v1.9.11, Zenodo, doi:10.5281/zenodo.8370018
 Brammer, G. B., van Dokkum, P. G., & Coppi, P. 2008, *ApJ*, **686**, 1503
 Bromm, V., & Loeb, A. 2003, *ApJ*, **596**, 34
 Campanelli, M., Lousto, C., Zlochower, Y., & Merritt, D. 2007, *ApJL*, **659**, L5
 Carniani, S., Hainline, K., D'Eugenio, F., et al. 2024, *Natur*, **633**, 318
 Casey, C. M., Kartaltepe, J. S., Drakos, N. E., et al. 2023, *ApJ*, **954**, 31
 Civano, F., Elvis, M., Lanzuisi, G., et al. 2010, *ApJ*, **717**, 209
 Civano, F., Marchesi, S., Comastri, A., et al. 2016, *ApJ*, **819**, 62
 Cleri, N. J., Olivier, G. M., Hutchison, T. A., et al. 2023, *ApJ*, **953**, 10
 Clowe, D., Bradač, M., Gonzalez, A. H., et al. 2006, *ApJL*, **648**, L109
 Corral, A., Della Ceca, R., Caccianiga, A., et al. 2011, *A&A*, **530**, A42
 Curtis-Lake, E., Carniani, S., Cameron, A., et al. 2023, *NatAs*, **7**, 622
 Deconto-Machado, A., Riffel, R. A., Ilha, G. S., et al. 2022, *A&A*, **659**, A131
 Delvecchio, I., Daddi, E., Sargent, M. T., et al. 2022, *A&A*, **668**, A81
 Dey, A., Schlegel, D. J., Lang, D., et al. 2019, *AJ*, **157**, 168
 Donnan, C. T., McLure, R. J., Dunlop, J. S., et al. 2024, *MNRAS*, **533**, 3222
 Ebisuzaki, T., Makino, J., Tsuru, T. G., et al. 2001, *ApJL*, **562**, L19
 Eisenstein, D. J., & Loeb, A. 1995, *ApJ*, **443**, 11
 Furtak, L. J., Labbé, I., Zitrin, A., et al. 2024, *Natur*, **628**, 57
 Gerber, R. A., Lamb, S. A., & Balsara, D. S. 1992, *ApJL*, **399**, L51
 Greene, J. E., & Ho, L. C. 2005, *ApJ*, **630**, 122
 Greene, J. E., Labbe, I., Goulding, A. D., et al. 2024, *ApJ*, **964**, 39
 Haehnelt, M. G., & Rees, M. J. 1993, *MNRAS*, **263**, 168
 Harikane, Y., Zhang, Y., Nakajima, K., et al. 2023, *ApJ*, **959**, 39
 Harrison, C. M., Thomson, A. P., Alexander, D. M., et al. 2015, *ApJ*, **800**, 45
 Hernquist, L., & Weil, M. L. 1993, *MNRAS*, **261**, 804
 Higdon, J. L. 1996, *ApJ*, **467**, 241
 Hoffman, L., & Loeb, A. 2007, *MNRAS*, **377**, 957
 Jain, R., & Wadadekar, Y. 2024, arXiv:2412.04834
 Jeon, J., Bromm, V., Liu, B., & Finkelstein, S. L. 2025, *ApJ*, **979**, 127
 Kauffmann, G., Heckman, T. M., Tremonti, C., et al. 2003, *MNRAS*, **346**, 1055
 Koekemoer, A. M., Faber, S. M., Ferguson, H. C., et al. 2011, *ApJS*, **197**, 36
 Krolik, J. H. 1999, *Active Galactic Nuclei: From the Central Black Hole to the Galactic Environment* (Princeton, NJ: Princeton Univ. Press)
 Labbé, I., van Dokkum, P., Nelson, E., et al. 2023, *Natur*, **616**, 266
 Lee, J., Shin, E.-j., & Kim, J.-h. 2021, *ApJL*, **917**, L15
 Lee, J., Shin, E.-j., Kim, J.-h., Shapiro, P. R., & Chung, E. 2024, *ApJ*, **966**, 72
 Lodato, G., & Natarajan, P. 2006, *MNRAS*, **371**, 1813
 Lousto, C. O., & Zlochower, Y. 2011, *PhRvD*, **83**, 024003
 Lynds, R., & Toomre, A. 1976, *ApJ*, **209**, 382
 Madau, P., & Rees, M. J. 2001, *ApJL*, **551**, L27

- Matthee, J., Naidu, R. P., Brammer, G., et al. 2024, *ApJ*, **963**, 129
- Mayer, L., Fiacconi, D., Bonoli, S., et al. 2015, *ApJ*, **810**, 51
- Mayer, L., Kazantzidis, S., Escala, A., & Callegari, S. 2010, *Natur*, **466**, 1082
- McConnell, N. J., & Ma, C.-P. 2013, *ApJ*, **764**, 184
- Mercier, W., Shuntov, M., Gavazzi, R., et al. 2024, *A&A*, **687**, A61
- Mezcua, M., Pacucci, F., Suh, H., Siudek, M., & Natarajan, P. 2024, *ApJL*, **966**, L30
- Momcheva, I. G., Brammer, G. B., van Dokkum, P. G., et al. 2016, *ApJS*, **225**, 27
- Morabito, L. K., Kondapally, R., Best, P. N., et al. 2025, *MNRAS*, **536**, L32
- Mowla, L., Iyer, K. G., Desprez, G., et al. 2022, *ApJL*, **937**, L35
- Mullaney, J. R., Alexander, D. M., Fine, S., et al. 2013, *MNRAS*, **433**, 622
- Natarajan, P. 2011, *BASI*, **39**, 145
- Natarajan, P., Pacucci, F., Ferrara, A., et al. 2017, *ApJ*, **838**, 117
- Natarajan, P., Pacucci, F., Ricarte, A., et al. 2024, *ApJL*, **960**, L1
- Negus, J., Comerford, J. M., Sánchez, F. M., et al. 2023, *ApJ*, **945**, 127
- Nelson, E. J., Suess, K. A., Bezanson, R., et al. 2023, *ApJL*, **948**, L18
- Netzer, H. 1990, in *Active Galactic Nuclei*, ed. R. D. Blandford et al. (Berlin: Springer), 57
- O’Dea, C. P. 1998, *PASP*, **110**, 493
- Peng, C. Y., Ho, L. C., Impey, C. D., & Rix, H.-W. 2002, *AJ*, **124**, 266
- Prochaska, J., Hennawi, J., Westfall, K., et al. 2020, *JOSS*, **5**, 2308
- Ricarte, A., Tremmel, M., Natarajan, P., Zimmer, C., & Quinn, T. 2021, *MNRAS*, **503**, 6098
- Saslaw, W. C., Valtonen, M. J., & Aarseth, S. J. 1974, *ApJ*, **190**, 253
- Schawinski, K., Urry, M., Treister, E., et al. 2011, *ApJL*, **743**, L37
- Scoville, N., Aussel, H., Brusa, M., et al. 2007, *ApJS*, **172**, 1
- Shin, E.-j., Jung, M., Kwon, G., et al. 2020, *ApJ*, **899**, 25
- Silk, J. 2019, *MNRAS*, **488**, L24
- Smirnov, D. V., Mosenkov, A. V., & Reshetnikov, V. P. 2024, *MNRAS*, **527**, 4112
- Smith, R. J., Lucey, J. R., & Carter, D. 2012, *MNRAS*, **426**, 2994
- Smolčić, V., Novak, M., Bondi, M., et al. 2020, COSMOS VLA 3GHz Catalog, IPAC, doi:10.26131/IRSA176
- Struck, C. 2010, *MNRAS*, **403**, 1516
- Tremmel, M., Governato, F., Volonteri, M., Pontzen, A., & Quinn, T. R. 2018, *ApJL*, **857**, L22
- Uppal, A., Ward, C., Gezari, S., et al. 2024, *ApJ*, **975**, 286
- Valentino, F., Brammer, G., Gould, K. M. L., et al. 2023, *ApJ*, **947**, 20
- van der Wel, A., Franx, M., van Dokkum, P. G., et al. 2014, *ApJ*, **788**, 28
- van Dokkum, P., Brammer, G., Wang, B., Leja, J., & Conroy, C. 2024, *NatAs*, **8**, 119
- van Dokkum, P., Pasha, I., Buzzo, M. L., et al. 2023, *ApJL*, **946**, L50
- van Dokkum, P., Shen, Z., Keim, M. A., et al. 2022, *Natur*, **605**, 435
- van Haarlem, M. P., Wise, M. W., Gunst, A. W., et al. 2013, *A&A*, **556**, A2
- Volonteri, M., Haardt, F., & Madau, P. 2003, *ApJ*, **582**, 559
- Wise, J. H., Regan, J. A., O’Shea, B. W., et al. 2019, *Natur*, **566**, 85